Determination of subshell-resolved *L*-shell-ionization cross sections of gold induced by 15–40-keV electrons

H. V. Rahangdale,[1,*] M. Guerra,[2] P. K. Das,[1] S. De,[1] J. P. Santos,[2] D. Mitra,[3] and S. Saha[1]

[1]*Applied Nuclear Physics Division, Saha Institute of Nuclear Physics, 1/AF, Bidhannagar, Kolkata-700064, India*

[2]*Centro de Física Atómica, CFA, Departamento de Física, Faculdade de Ciências e Tecnologia, FCT, Universidade Nova de Lisboa, 2829-516 Caparica, Portugal*

[3]*Department of Physics, University of Kalyani, Kalyani, Nadia-741235, India*

(Received 20 February 2014; published 14 May 2014)

The L-subshell specific electron impact ionization cross sections, near the ionization threshold ($15 < E < 40$ keV) of gold are calculated from the measured production cross sections in this collaborative work between an experimental and a theoretical group. Calculations are performed using the distorted wave Born approximation formalism, and the modified relativistic binary encounter Bethe model to understand the data. The observed agreements and discrepancies between the two theoretical formalisms considered and the experimental data are reported.

DOI: 10.1103/PhysRevA.89.052708 PACS number(s): 34.80.Dp, 34.50.Fa, 36.20.Kd

I. INTRODUCTION

Electron impact excitation is established as an important probe for exploring the structure of matter. While penetrating through matter, electrons, positrons, and photons at high energy, suffer multiple collisions and lose energy at each step of the process. Depending on the beam energy, they originate the emission of secondary particles (electrons, positrons, photons) and undergo multiple interactions that promote the energy transfer to the atoms and molecules of the penetrating medium. At electron impact energies near the atomic binding energies (a few eV to tens of keV), ionization and subsequent rearrangement of atomic electrons take place, resulting in emission of photons. While the underlying interactions responsible for the process are the Coulomb and the exchange interactions, the presence of multiple electrons, both bound and those belonging to the continuum, complicate the dynamics of the collision process, and therefore, subsequent results or the observable effects are not fully understood in all the experiments. As a result, the effective theories for the multielectron systems quite often depend on parameters which are not unique. These parameters to a greater extent are dependent on the atomic structure, and to a lesser extent on the collective nature of the medium.

Electron impact ionization data is of great importance in many applications like electron probe microanalysis (EPMA), electron energy loss spectroscopy (EELS), Auger electron spectroscopy (AES), which are widely used in material characterization. In fact, the inner-shell-ionization cross-section data are essential in sensitivity analysis, choice of detector configuration (e.g., detection techniques to be used, type of materials, and thicknesses to be used as absorber, etc.), and the detection strategies to be incorporated into such analytical instruments [1]. Electron transport simulations, which are essential in the field of medical science, particularly in electron linac-based medical imaging, diagnosis, and cancer therapy, require a reliable cross-section database for error-free patient management [2]. These important applied areas, thus, require electron impact ionization cross-section data for different targets over a continuous, wide range of energy values, and with an acceptable accuracy.

In the field of x-ray astronomy, the importance of atomic data need not be over-emphasized. There are many features in the x-ray band of the emitted photons that require detailed knowledge of the collisional transition rates and the radiative transition rates of the constituent systems. Since the astronomical sources that emit x rays (usually the supernova remnants in various galaxies) are far from thermodynamic equilibrium, the instruments or detection systems used in space stations and in space-borne x-ray telescopes with even the highest resolving power are not capable of fully resolving the x-ray lines due to the above reason. The field of observational astronomy has evolved rapidly, so that collisional model-based interpretation of a wide range of data assumes particular significance [3]. In this context, benchmarking these models with laboratory-based measurements, such as the ones attempted in this work, becomes all the more relevant.

Development of theoretical formalisms, or models, to describe the electron impact ionization has gone through a rapid progress, which can be categorized in two segments. In one segment, theoretical estimates of the total cross section under the single ionization condition are attempted. The Lotz formula [4] was one of the first empirical formulas of this kind, where the used parameters were obtained by fitting experimental data over a limited range of light mass elements (He to Ca). The Deutsch Mark formalism [5], which was put forth as an extension of the capabilities of cross-section calculations have also found limited use to explain experimental data, particularly for the L shell and beyond. *Ab initio* convergent close coupling (CCC) calculations [6], including relativistic effects, have been developed in recent times to treat the electron-atom or ion-atom interactions as time-dependent scattering problems. The total ionization cross sections are estimated from the scattering probabilities. Though the results are expected to be more in agreement with the experimental data, the estimate of subshell-resolved ionization cross sections will take some more time to reach a

*hitesh.rahangdale@saha.ac.in

reliable level. Theoretical calculations, categorized into the other segment, are the ones that attempt to calculate the subshell-resolved cross sections, which can be benchmarked by the experiments carried out in this work. The plane-wave Born approximation (PWBA) calculations, with corrections for Coulomb, relativistic, and exchange effects, have been found to be in good agreement with the K-shell- and L-subshell-ionization cross sections (L_1, L_2, L_3) for energies from 50 to 600 keV [7]. However, the PWBA theory fails to account for the cross section and their energy dependence at lower energies. Besides, at lower energies ($\lesssim$50 keV), the plane-wave approximation to scattering formalism will not hold true and the relativistic corrections are expected to be negligible. At energies near the ionization threshold (typically at $T \lesssim 20U$, where T and U are the kinetic energy and the ionization threshold, respectively), the distortion of the wave functions from plane wave towards a spherical wave, due to the electrostatic field of the atoms, needs to be considered. The distorted wave Born approximation (DWBA) calculations, taking relativistic effects and exchange interaction into account, were successfully used to estimate the K-, L-, and M-shell-ionization cross section for the atoms [8]. At higher energies (typically $T \gtrsim 20U$), the PWBA cross sections are multiplied by an energy-dependent scaling factor that becomes unity at energies where PWBA theory gives good agreement with experimental data. The above formalism of theoretical estimates based on DWBA and PWBA have been incorporated in the computer code PENELOPE [9]. Comparison of DWBA cross section estimates with the experimental data is attempted in this work. Recently, the binary encounter Bethe (BEB)-model-based formalism, like the modified relativistic binary encounter Bethe (MRBEB) model [10] has been successful in estimating the K- and L-shell-ionization cross sections. The model involves a single external parameter, *viz.* the binding energy of the electrons in the neutral atom to be ionized and also uses a scaling factor to account for energy dependence across the energy scale to include the effects due to electron exchange, polarization, and distortion of wave functions. The MRBEB method, thus, generates direct ionization cross-section curves for neutral atoms ($6 < Z < 83$), which are reliable in intensity ($\pm$20%) and shape from the ionization threshold to thousands of keV. Benchmarking the MRBEB-model-based estimates is an important aspect of the present work.

Earlier experiments on electron impact ionization studies focused primarily on the K-shell-ionization cross section, while L- and M-shell-ionization data were seldom reported [11]. Recently, many authors have reported L x-ray production cross sections for a few elements, and validation of various theoretical models are done using the data. Comparison between theory and various experiments on L-shell production cross sections in a few heavy elements ($72 \leqslant Z \leqslant 83$) were done by Fernandez-Varea *et al.* [12] and also by Wu *et al.* [13]. These results are revisited and extended further for gold in this work.

A review of the existing L-shell-ionization cross-section data for gold reveals that, while the x-ray production cross sections by electron impact were reported quite a few times over the past decades, the reporting of subshell-specific ionization cross sections was rarely found near the ionization threshold region. Studies reported by earlier researchers were either restricted to very few electron impact energy [14], or were inaccurate due to not taking Coster-Kronig transitions into account [15,16]. First systematic studies by Palinkas and Schlenk [17] reported $L_\alpha, L_\beta, L_\gamma$ production cross sections and obtained L_1, L_2, L_3 ionization cross sections in the energy range 60–600 keV. Shima *et al.* [18] did experiments near ionization threshold and reported $L_\alpha, L_\beta, L_\gamma$ production cross sections and L_3 ionization cross section. Schneider *et al.* [19] had reported L_3 ionization cross section by electron and positron impact near the ionization threshold. Recent experiments done by Campos *et al.* [20] and Wu *et al.* [13] provided improved results for L_α and L_β production cross sections but no result for the L_γ line.

In the present work, we have measured the $L_\alpha, L_\beta, L_\gamma$ production cross sections in gold, and converted the obtained values to the subshell-specific ionization cross sections. The experimental data are compared with the MRBEB values calculated in this work and with the theoretical calculations based on the (DWBA) obtained from PENELOPE [21]. To the best of our knowledge, the subshell-specific ionization cross section for the L shell of gold are reported here for the first time at the energy values near the corresponding ionization threshold.

II. EXPERIMENTAL DETAILS

The schematic of the experimental setup used is shown in Fig. 1. It consists of an electron gun, capable of delivering a 1–50-keV electron beam of up to 100 μA current (Kimball Physics, USA). The electron beam can be focused using electromagnetic lenses to a spot size of 0.5–10 mm up to a distance of 600 mm from the exit port of the gun. The electron gun is mounted on the horizontal central plane of a cylindrical stainless steel (SS-304) vacuum chamber consisting of four DN-100CF vacuum ports, with two ports placed 180° apart. The electron gun is attached to one of the ports and a Faraday cup on the other. The Faraday cup, made of aluminium alloy, is designed as a cylindrical cuplike structure, ending up in a conical block with a vertex angle ~60°) to reduce the

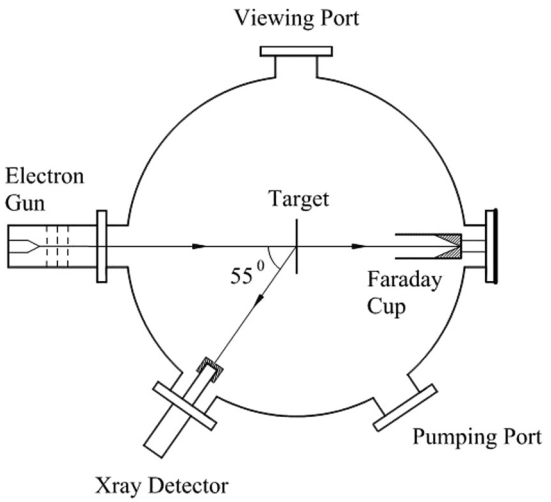

FIG. 1. Schematic diagram of the experiment.

back-scattering loss of the electrons. The gun and the Faraday cup are aligned using a laser-based beam aligner such that the axis defined by the two elements, passes through the chamber center. Small misalignment and deviation of the beam due to the remnant magnetic field (relevant for operation at low energy) can be rectified using corrector permanent magnets placed outside the chamber.

Thin targets, made of different materials and mounted on a target ladder, are placed at the center of the chamber. The target ladder, placed vertically at the center, is mounted on a stainless steel rod which passes through a Wilson seal vacuum feedthrough. The desired target can be placed at the central plane with the target center coinciding on the electron beam axis by adjusting the position of the ladder. The ladder consists of five mounting positions, with two positions occupied by (1) a thin silver doped zinc sulfide coated phosphor screen and (2) a blank target frame, leaving three positions to mount targets. Thin targets of thickness ∼50–150 $\mu g\,cm^{-2}$, self-supporting or backed by a 20 $\mu g\,cm^{-2}$ carbon foil, and mounted on an aluminium frame, are used. The choice of aluminium frame is to have K x rays produced by beam halo, to be nonoverlapping with most of the characteristic L x-ray lines to be studied in this experiment.

The characteristic x rays emitted from the target are detected by a cryogen-free PIN diode x-ray detector (model No. XR-100CR from Amptek, USA) used as energy dispersive spectrometer. The detector, with an effective area of 13 mm^2, has a thin (25.4-μm) beryllium window causing cutoff below ∼1-keV x rays. To avoid attenuation of x rays below 10 keV, the detector with its built-in preamplifier and the Peltier cooler, was mounted inside the SS vacuum chamber on an aluminium block, which is mounted from the DN-100 CF flange such that the detector views the target center sitting at the 125° angle with respect to the upstream electron beam. The active region of the detector is shielded from the scattered x rays by a graded collimator of cylindrical shape and having an axial opening hole of 2 mm. The collimator has four different layers made of elements with decreasing atomic number (Z) from the outer surface to the inner one. The outer shell is made of lead, followed by shells of copper, aluminium, and graphite. The collimator efficiently shields the active element of the detector as observed from the overall reduction of the spectral background. The front surface of the collimator is covered with a mylar foil (100-μm thick) to cut off x rays below ∼5 keV. Apart from reducing the low energy x-ray background, it significantly reduces the dead time loss of the data acquisition system. From the available data on x-ray attenuation in Mylar [22], the chosen absorber cuts ∼83.8% of x rays below 3 keV and ∼99.8% of x rays below 2 keV. The distance between target center and the detector collimator entrance is 77 mm. Thus, the detector subtends a solid angle of $\sim 5.3 \times 10^{-4}$ steradian at the target center. The preamplifier output from the x-ray detector is fed to the input of a shaping amplifier (25-μs shaping time), whose output goes to a multichannel analyzer (model Oxford WIN-MCA, American Nuclear System) with 8-k analog to digital converter (ADC).

The total efficiency (ϵ) of the detector is an important parameter needed for the experiment. It was determined for nonoverlapping lines by two different methods. Characteristic x-ray lines from a calibrated ^{241}Am source (37 kBq) were used to determine the yield. In another method, copper K x-ray yields due to electron beam bombardment at known energy on a copper target of predetermined thickness and purity were used [23]. The efficiency plot obtained is shown in Fig. 2. The efficiency data were fitted with a second order polynomial function: $\epsilon(E) = 1.58 \times 10^{-5} + 1.31 \times 10^{-6}E - 8.63 \times 10^{-8}E^2$. The overall fitting error, optimized by χ^2 minimization, was found to be ∼10%.

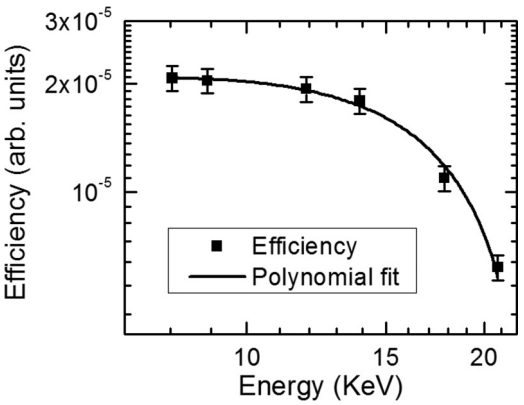

FIG. 2. Efficiency of the PIN diode x-ray detector used in the experiment.

Two more important parameters involved in a typical in-beam cross-section measurement are the beam flux impinging on the target and the target thickness. The beam current in the experimental setup was measured by a deep Faraday cup. The method basically boils down to (1) efficient collection of the electrons from the beam, (2) reduction of loss due to the backscattered electrons, and (3) account for loss of electrons from the target. The Faraday cup was cylindrical in shape with a length of 210 mm and an opening diameter of 80 mm. The base of the Faraday cup was made conical to ensure trapping of secondary electrons in the Faraday cup itself. The opening angle of the cone was ∼60°. The collection efficiency was checked by biasing the Faraday cup at +105 V with respect to the chamber held at ground potential. The collected current was at the most 3% higher due to biasing. The collection efficiency was also checked by applying a negative potential to a copper ring mounted at the face of the Faraday cup. No significant difference was observed even after biasing the ring by −1000 V.

The current at the target ladder during the beam-on condition was measured by insulating the target ladder from the main chamber. The target ladder was biased to +105 V. With the target in the beam position, the total beam current is the sum of current measured at the Faraday cup and that at the target ladder. This total beam current was not equal to the beam current collected by the Faraday cup when the target was out of the beam. This deficiency in current was because of the backscattering of the electrons from the target. One can use the backscattering factor to get the actual number of incident electrons, but this data is not always available for the required thickness, and hence one has to rely on estimated values, which may vary by 10%–20% [24]. To avoid the backscattering factor correction, the total number of electrons during a given time was measured using the charges collected

at the Faraday cup with and without the target. This ratio was measured throughout experiment at regular intervals and found that the variation was $\lesssim 1\%$. To get the actual number of electrons in the beam, the total integrated charge during the data collection period was scaled by this ratio.

The target thickness in this measurement is another important parameter to be known accurately. The targets are expected to be thin so as to achieve a single collision condition and minimize multiple scattering on the target, but they should also be thick enough to give moderate count rates. In general, the single collision condition is satisfied if $n\sigma \lesssim 1$ where n is the number of target atoms per cm^2 and σ is the cross section. The thin targets used in the experiment were prepared by the electron beam vapor deposition (EBVD) technique. The target thickness was obtained by measuring the energy loss of monoenergetic alpha particles while passing through the target. The thickness measurement was done in a separate vacuum chamber in which, a mixed alpha source containing ^{239}Pu, ^{241}Am, and ^{244}Cm, the target, and a silicon surface barrier detector were placed in a straight line. Base pressure of 10^{-2} mbar or better was maintained in the chamber. This energy loss was converted into thickness using the stopping power dE/dx of the alpha particles in the target materials using the well-known code SRIM [25]. The gold target (purity 99.99%) used in the experiment was found to be of $156.0 \pm 7.5\ \mu$g cm^{-2} thickness.

In the experiment, data were collected with monoenergetic electron beam of spot size 2 mm, at 11 different energies in the range 16–40 keV at approximately 2–3-keV intervals. Typical data collection time for each run was ~4–5 h. Data acquisition conditions were such that the count rate was below 200 cps and the beam current was less than a few tens of nanoampere for all the electron energies. Due to the high input count rate handling capacity of the detector (>50 kcps) and low electron beam current, the dead time was negligible ($\lesssim 1\%$).

A. Data analysis

The typical x-ray spectrum of gold by electron impact at 25-keV electron beam energy is shown in Fig. 3(a). Each of the L_α,L_β, and L_γ lines of gold were fitted separately with the Gaussian profile and a linear background using the least square fitting program. Net count for a particular line was obtained by subtracting total count under the interpolated linear baseline from the integral count under the peak. The net count was corrected for self-absorption in the target itself. Self-absorption correction was done assuming that x rays were created midway in the target and moved backward along 125° to reach the detector. The attenuation coefficients were taken from [22], and the correction was less than 2%. No correction for the pile-up effect and MCA dead time was required because of the very low count rate. The total count for each x-ray peak was converted into the respective production cross section using the well-known formula,

$$\sigma_i(E) = \frac{N_X A}{\epsilon(E')tN_e N_A}, \tag{1}$$

where $\sigma_i(E)$ is the production cross section (cm^2) of L_i line at electron energy E, N_X is the total number of x rays for the particular line, A is the atomic mass of the target, $\epsilon(E')$ is the effective efficiency of the detector at photon energy E', t is the mass thickness of target(g/cm^2), N_e is the number of electrons, and N_A is the Avogadro number.

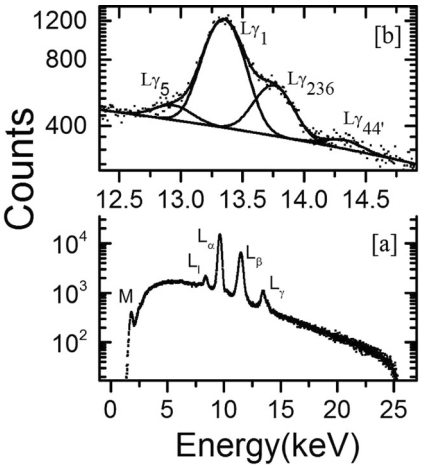

FIG. 3. (a) Typical spectrum at 25-keV electron impact energy. (b) Fitting of L_γ peaks from the spectrum taken at 40-keV electron impact energy.

The effective efficiency of the detector includes the geometric factor, the intrinsic efficiency, and the absorption correction for Mylar. Also, there was no enhancement in the net count of a peak due to the bremsstrahlung photons created inside the target. This was confirmed by calculating the number of vacancies created by the total bremsstrahlung photons whose energy was higher than the shell excitation energy. The required photoionization cross sections were taken from XCOM [26].

To compare with theory, the experimentally obtained production cross sections were converted to the ionization cross sections using Eqs. (2), (3), and (5) [27], given as

$$\sigma_{L_{\gamma_{2+3}}} = \sigma_{L_1}\omega_1 S_{\gamma_{2+3,1}}, \tag{2}$$

$$\sigma_{L_{\gamma_{1+5}}} = \left[\sigma_{L_1} f_{12} + \sigma_{L_2}\right]\omega_2 S_{\gamma_{1+5,2}}, \tag{3}$$

$$\begin{aligned}\sigma_{L_\beta} = {} & \sigma_{L_1}[\omega_1 S_{\beta,1} + \omega_2 f_{12} S_{\beta,2} + \omega_3(f_{13} + f_{12}f_{23})S_{\beta,3}] \\ & + \sigma_{L_2}(\omega_2 S_{\beta,2} + \omega_3 f_{23} S_{\beta,3}) + \sigma_{L_3}\omega_3 S_{\beta,3},\end{aligned} \tag{4}$$

$$\sigma_{L_\alpha} = \left[\sigma_{L_1}(f_{12}f_{23} + f_{13}) + \sigma_{L_2} f_{23} + \sigma_{L_3}\right]\omega_3 S_{\alpha,3}. \tag{5}$$

Here, $S_{i,I}$ is the fraction of radiative transition to the I^{th} subshell associated with the L_i peak, f_{ij}'s are the Coster-Kronig transition probabilities between subshells L_i and L_j, and ω_i's are the fluorescence yields corresponding to subshells L_i. In the above equations, we have used only production cross sections of the $L_{\gamma_{1,2,3,5}}$ and L_α lines, which is the best possible combination according to [27]. The same reference

TABLE I. Fluorescence yield and Coster-Kronig transition probabilities.

	ω_1	ω_2	ω_3	f_{12}	f_{13}	f_{23}
Campbell [30]	0.13	0.358	0.313	0.07	0.58	0.125
Krause [31]	0.107	0.334	0.32	0.14	0.53	0.122

TABLE II. Radiative yields taken from Campbell and Wang [28].

Initital subshell	Radiative yield for final subshell									Total
	M1	M4	M5	N1	N4	N5	O1	O45	P1	
L3	0.0686	0.1389	1.221	0.017	0.0268	0.2412	0.0034	0.0271	0.0002	1.744
	M1	M4	N1	N4	O1	O4	P1			
L2	0.0432	1.574	0.0111	0.3288	0.0022	0.0347	0.0001			1.9942
	L3	M2	M3	N2	N3	O23				
L1	0.0297	0.3745	0.4339	0.097	0.1226	0.0391				1.0968

also suggests other combinations to find the ionization cross sections.

For converting production cross sections into ionization cross sections, it was necessary to properly de-convolute the L_γ peak. The L_γ line of the spectra was fitted with the L_{γ_5}, L_{γ_1}, $L_{\gamma_{236}}$, and $L_{\gamma_{44'}}$ lines for electron energy of 20 keV and above, but for 16- and 18-keV electron energies, only L_{γ_1} and $L_{\gamma_{236}}$ could be resolved. The processed L_γ spectrum at 40 keV is shown in Fig. 3(b).

The production cross sections for the $L_{\gamma_{2+3}}$ line required as input to Eq. (2) was obtained by subtracting the contribution of the L_{γ_6} line from the fitted $L_{\gamma_{236}}$ peak. The L_{γ_6} line contribution was obtained using the ratio $\Gamma_{\gamma_6}/\Gamma_{\gamma_1}$ and L_{γ_1} peak counts from the fitted spectrum. Here Γ_{γ_6} and Γ_{γ_1} are the radiative yields of the γ_6 and γ_1 lines, respectively, which were taken from [28,29]. Two sets of atomic parameters were taken for comparison with theoretical predictions. The first set consists of fluorescence yield from Campbell [30] and radiative yield from Campbell and Wang [28]. The first set is based on theoretically calculated values while the second set is a collection of classical values compiled by Krause (fluorescence yield) [31] and Scofield (radiative yields) [29]. Tables I–III enlist all the parameters that were used.

III. RESULTS AND DISCUSSION

The experimental results were compared with the theoretical estimates in order to understand their merits and demerits in predicting the L x-ray cross sections in this target element and electron energy regime. Two different theoretical formalisms were used for the purpose, *viz.* the MRBEB and DWBA.

The MRBEB method involves calculation of direct ionization cross sections for the neutral atoms with modification of the energy-dependent scaling term, which depends on the kinetic energy and the binding energy of the electrons in the specific subshell, designated by nlj, where the symbols carry their usual meaning. The merit of the MRBEB theory lies in the fact that it requires only one parameter, *viz.* the binding energy of the inner shell electrons. The corresponding cross sections for direct ionization of an nlj bound electron of binding energy B in an atom in the initial state LS (where L and S are the orbital angular momentum and the spin angular momentum, respectively) by an incident electron with kinetic energy T reads [10]

$$\begin{aligned}\sigma_{\mathrm{MRBEB},n\ell jLS} = &\left(1+f\left(\frac{Z_{\mathrm{eff}}}{tZ}\right)^{\lambda}\right)\frac{4\pi a_0^2\alpha^4 N_{n\ell j}}{\left(\beta_t^2+\chi_{n\ell j}\beta_b^2\right)2b'}\\ &\times\left\{\frac{1}{2}\left[\ln\left(\frac{\beta_t^2}{1-\beta_t^2}\right)-\beta_t^2-\ln(2b')\right]\right.\\ &\times\left(1-\frac{1}{t^2}\right)+1-\frac{1}{t}-\frac{\ln t}{t+1}\frac{1+2t'}{(1+t'/2)^2}\\ &\left.+\frac{b'^2}{(1+t'/2)^2}\frac{t-1}{2}\right\},\end{aligned} \tag{6}$$

where

$$\begin{aligned}\beta_t^2 &= 1-\frac{1}{(1+t')^2} \quad t' = T/mc^2,\\ \beta_b^2 &= 1-\frac{1}{(1+b')^2} \quad b' = B/mc^2,\\ t &= T/B \quad \chi_{n\ell j} = (X_{n\ell j}/B)2R.\end{aligned} \tag{7}$$

Here, c is the speed of light in vacuum, $X_{n\ell j}$ is a scaling constant related to the potential energy of the incident electron in the ionization region, R is the Rydberg energy (13.6 eV), m is the electron mass, and Z_{eff} is the effective charge of the orbital undergoing ionization. In Eq. (6), α is the fine structure constant, $N_{n\ell j}$ is the subshell occupation number, a_0 is the Bohr's radius in meters, and the parameters f and λ in the ionic correction factor that scales the MRBEB expression, are $f = 3$ and $\lambda = 1.27$ [32]. The energy values are in the same units. The B parameter can be obtained either from the compiled experimental values or from the theoretical values estimated using Dirac-Fock wave functions which are reliable

TABLE III. Radiative yields taken from Scofield [29].

Initital subshell	Radiative yield for final subshell									Total
	M1	M4	M5	N1	N4	N5	O1	O4,5	P1	
L3	0.0680	0.1377	1.2140	0.0166	0.0252	0.2267	0.0033	0.0225	0.0001	1.7108
	M1	M4	N1	N4	O1	O4	P1			
L2	0.0423	1.5650	0.0108	0.3090	0.0022	0.0291	0.0001			1.9618
	L3	M2	M3	N2	N3	O2	O3			
L1	0.0289	0.3730	0.4300	0.0943	0.1173	0.0169	0.0204			1.1172

TABLE IV. Experimental production and ionization cross sections of Au. Ionization cross sections are obtained using the relaxation parameter [28,30].

	Production cross section			Ionization cross section		
Energy (KeV)	L_α (barn)	L_β (barn)	L_γ (barn)	L_1 (barn)	L_2 (barn)	L_3 (barn)
16	91.1(9.1)	35.5(4.0)	2.9(0.3)	7.3(2.2)	39.0(4.4)	364.2(41.6)
18	116.3(11.6)	55.8(6.2)	6.5(0.7)	25.7(5.7)	84.5(9.3)	450.6(53.1)
20	144.2(14.4)	74.4(8.3)	8.6(1.0)	39.9(8.0)	110.5(11.9)	553.5(65.9)
23	160.6(16.1)	84.7(9.4)	11.0(1.2)	48.1(9.7)	142.6(14.6)	611.9(73.5)
25	168.9(16.9)	91.9(10.2)	12.3(1.4)	52.9(10.7)	159.5(16.4)	641.1(77.3)
28	173.4(17.3)	93.9(10.5)	12.6(1.4)	56.5(11.3)	161.9(16.8)	657.1(79.4)
30	166.6(16.7)	93.0(10.4)	12.4(1.4)	60.1(11.6)	158.2(16.7)	627.3(76.3)
33	170.3(17.0)	96.4(10.7)	13.2(1.5)	60.1(11.8)	170.5(17.4)	641.1(78.0)
35	162.6(16.3)	92.2(10.3)	11.9(1.3)	66.6(12.0)	147.6(15.8)	608.4(74.5)
38	158.6(15.9)	90.5(10.1)	12.7(1.4)	58.3(11.5)	162.5(17.0)	595.4(72.7)
40	171.7(17.2)	99.3(11.1)	13.1(1.5)	71.6(13.0)	163.1(17.4)	641.1(78.7)

within ∼1%. Further details of the theoretical model can be found in Refs. [10,33].

Theoretical cross sections using DWBA formalism, including relativistic effects and the effects of both distortion and exchange, is incorporated in the modified code PENELOPE [21]. DWBA calculations yield total cross sections in fairly good agreement with experimental data for the ionization of K and L shells. These calculations involve the expansion of wave functions as partial wave series and the subsequent evaluation of multiple radial integrals. Since the convergence of the partial-wave series becomes very slow at higher kinetic energies, DWBA calculations are feasible only for projectiles with relatively small energies, up to about $20U$ (U being the ionization threshold). DWBA calculations for the neutral atoms involving relativistic corrections were done by Segui *et al.* [34]. The DWBA calculations done by Bote *et al.* [23] were included in the PENELOPE code. Further details are available in Ref. [34].

The x-ray production cross sections, obtained from the experiment are shown in Table IV. Ionization cross sections, derived from the production cross sections are displayed in the same table. Uncertainties in the values are indicated. The overall uncertainties in the L x-ray production cross sections are ∼11%–12%. Major contributions to the uncertainties come from the detector efficiency(10%), beam current measurement (∼3%), and the target thickness measurement (∼5%). However, the uncertainties in the corresponding ionization cross sections are a bit larger due to propagation of errors as per Eqs. (2), (3), and (5), more specifically, it is relatively larger for the L_1 subshell and smaller for L_2 and L_3.

The L x-ray production cross sections, obtained in this experiment and also those measured by Wu *et al.* [13] and Shima *et al.* [18], are plotted in Fig. 4. MRBEB and DWBA results are also plotted in the same graph. It can be seen that the MRBEB and DWBA predictions agree with experimental results for L_α and L_β up to $E \sim 15$ keV. For $E > 15$ keV, DWBA results are in good agreement with all three experiments for L_α, but the MRBEB theory overpredicts the L_α cross sections in this energy domain. For the L_β line, the DWBA results are in reasonable agreement with the experiments for $15 < E < 25$ keV, but overpredicts by ∼30% at higher energies. Unfortunately, our results are the only one in this energy domain. The same tendency of mismatch at similar electron energy domain was also observed in Pb [35] and Bi [36] as well. MRBEB overpredicts the L_β cross sections for $E > 15$ keV. Both the theories overpredict the L_γ cross sections over the entire electron kinetic energy range, though the experimental results of Shima *et al.* [18] match with DWBA within the uncertainties of their data, which are relatively larger than in the present experiment.

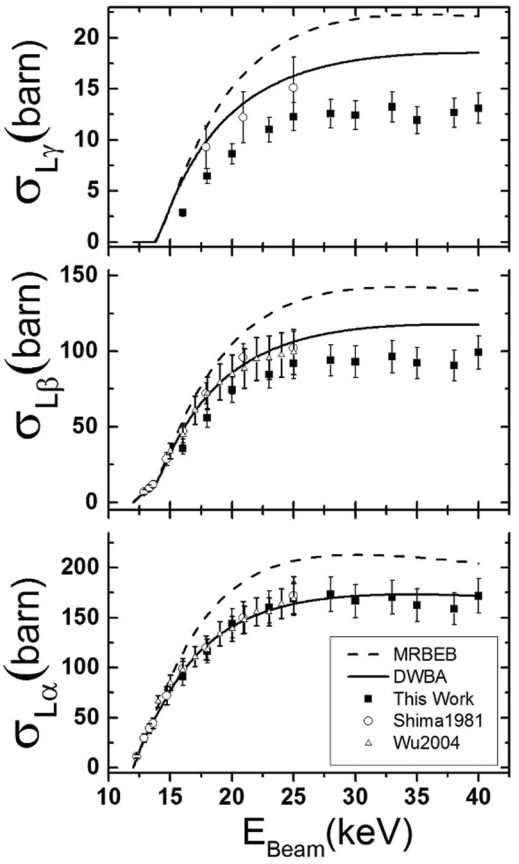

FIG. 4. Production cross section of L_α, L_β, and L_γ lines of Au. Theoretical values are obtained using relaxation parameters [28,30].

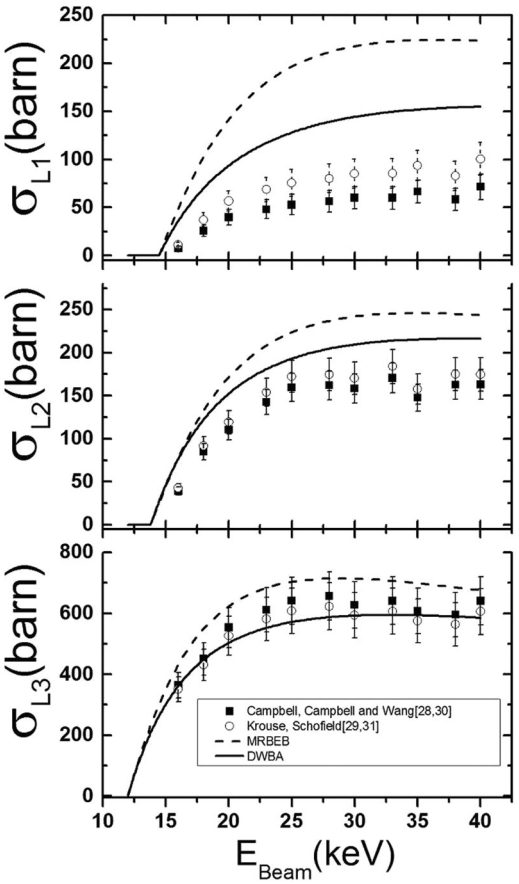

FIG. 5. L_1, L_2, and L_3 subshell ionization cross sections of gold.

For a consistent comparison of the experimental results, including parameter dependence, the production cross sections are converted to ionization cross sections using two different sets of atomic parameters. The results, along with those from the MRBEB and DWBA calculations, are plotted in Fig. 5. While the parameter-dependent variation is ∼30% for σ_{L1}, it is relatively less (∼10%) for σ_{L2} and σ_{L3}. On the other hand, the discrepancy between experiment and both the theories appears to be the largest for L_1, and a significant but smaller discrepancy for the DWBA than for the MRBEB formalism. There is a reasonable agreement between both the theories and the experimental results for L_3 within the uncertainty limits.

IV. CONCLUSIONS

The L-subshell-specific electron impact ionization and production cross sections near the ionization threshold ($15 < E < 40$ keV) of gold were measured. Also, the L_γ production cross sections by electron impact in one of the high Z elements is reported. The discrepancy between the two theoretical formalisms considered (DWBA and MRBEB) and experimental data reported in this work indicate the need for more experimental data, and a detailed look at the dynamical processes involved in electron impact ionization to identify the role of the atomic parameters used as links between theoretical formalisms and the experimental results. The widening of discrepancy between experimental results and theoretical estimates at relatively higher energies also points to the possibilities of multidimensional and/or multichannel couplings into play in deciding the effective connections between the production cross sections and the subshell-specific ionization probabilities. Further investigation in this direction is essential to solve the discrepancies and understand the mechanism of inner-shell ionization in more detail.

ACKNOWLEDGMENTS

This research work is supported by the Department of Atomic Energy, Government of India. Two of the authors (M.G. and J.P.S.) would like to acknowledge research support in part by Fundação para a Ciência e a Tecnologia (FCT), Portugal, through the Projects No. PEstOE/FIS/UI0303/2011 and No. PTDC/FIS/117606/2010, financed by the European Community Fund FEDER through the COMPETE. The authors acknowledge the fabrication of the experimental setup by the SINP machine shop.

[1] C. J. Powell, Rev. Mod. Phys. **48**, 33 (1976).
[2] M. R. Ay, S. Sarkar, M. Shahriari, D. Sardari, and H. Zaidi, Med. Phys. **32**, 1660 (2005).
[3] T. R. Kallman and P. Palmeri, Rev. Mod. Phys. **79**, 79 (2007).
[4] W. Lotz, Zeitschrift fr Physik **216**, 241 (1968).
[5] A. K. F. Haque, M. S. I. Sarker, M. A. R. Patoary, M. Shahjahan, M. I. Hossain, M. A. Uddin, A. K. Basak, and B. C. Saha, Int. J. Quantum Chem. **109**, 1442 (2009).
[6] M. S. Pindzola, J. A. Ludlow, F. Robicheaux, J. Colgan, and C. J. Fontes, Phys. Rev. A **80**, 052706 (2009).
[7] S. P. Khare and J. M. Wadehra, Can. J. Phys. **74**, 376 (1996).
[8] D. Bote and F. Salvat, Phys. Rev. A **77**, 042701 (2008).
[9] J. Bar, J. Sempau, J. Fernndez-Varea, and F. Salvat, Nuclear Instruments and Methods in Physics Research Section B: Beam Interactions with Materials and Atoms **100**, 31 (1995).
[10] M. Guerra, F. Parente, P. Indelicato, and J. Santos, Int. J. Mass Spectrom. **313**, 1 (2012).
[11] D. C. Joy, Scanning **17**, 270 (1995).
[12] J. M. Fernández-Varea, S. Segui, and M. Dingfelder, Phys. Rev. A **83**, 022702 (2011).
[13] Y. Wu, Z. An, M. T. Liu, Y. M. Duan, C. H. Tang, and Z. M. Luo, J. Phys. B: At. Mol. Opt. Phys. **37**, 4527 (2004).
[14] S. Salem and L. Moreland, Phys. Lett. A **37**, 161 (1971).
[15] M. Green and V. E. Cosslett, J. Phys. D **1**, 425 (1968).
[16] D. Davis, V. Mistry, and C. Quarles, Phys. Lett. A **38**, 169 (1972).
[17] J. Plinks and B. Schlenk, Zeitschrift fr Physik A Atoms and Nuclei **297**, 29 (1980).
[18] K. Shima, T. Nakagawa, K. Umetani, and T. Mikumo, Phys. Rev. A **24**, 72 (1981).
[19] H. Schneider, I. Tobehn, F. Ebel, and R. Hippler, Phys. Rev. Lett. **71**, 2707 (1993).
[20] C. S. Campos, M. A. Z. Vasconcellos, X. Llovet, and F. Salvat, Phys. Rev. A **66**, 012719 (2002).

[21] http://www.oecd-nea.org/lists/penelope.html
[22] http://henke.lbl.gov/optical_constants/filter2.html
[23] D. Bote, F. Salvat, A. Jablonski, and C. J. Powell, At. Data Nucl. Data Tables **95**, 871 (2009).
[24] W. Williamson and A. J. Antolak, J. Appl. Phys. **61**, 4880 (1987).
[25] http://www.srim.org
[26] http://www.nist.gov/pml/data/xcom/index.cfm.
[27] G. Lapicki, A. C. Mandal, S. Santra, D. Mitra, M. Sarkar, D. Bhattacharya, P. Sen, L. Sarkadi, and D. Trautmann, Phys. Rev. A **72**, 022729 (2005).
[28] J. Campbell and J.-X. Wang, At. Data Nucl. Data Tables **43**, 281 (1989).
[29] J. H. Scofield, At. Data Nucl. Data Tables **14**, 121 (1974).
[30] J. Campbell, At. Data Nucl. Data Tables **85**, 291 (2003).
[31] M. O. Krause, J. Phys. Chem. Ref. Data **8**, 307 (1979).
[32] A. Haque, M. Hossain, T. Talukder, M. Hasan, M. Uddin, A. Basak, B. Saha, and F. Malik, Radiat. Phys. Chem. **91**, 50 (2013).
[33] M. Guerra, F. Parente, and J. Santos, Int. J. Mass Spectrom. **348**, 1 (2013).
[34] S. Segui, M. Dingfelder, and F. Salvat, Phys. Rev. A **67**, 062710 (2003).
[35] A. Moy, C. Merlet, X. Llovet, and O. Dugne, J. Phys. B: At. Mol. Opt. Phys. **46**, 115202 (2013).
[36] Y. Wu, Z. An, Y. Duan, and M. Liu, Nuclear Instruments and Methods in Physics Research Section B: Beam Interactions with Materials and Atoms **268**, 2473 (2010).